Photoacoustics 3 (2015) 107–113

Contents lists available at ScienceDirect

Photoacoustics

journal homepage: www.elsevier.com/locate/pacs

Sensing the delivery and endocytosis of nanoparticles using magneto-photo-acoustic imaging

M. Qu, M. Mehrmohammadi [1], S.Y. Emelianov [2,*]

Department of Biomedical Engineering, University of Texas at Austin, 107 W Dean Keeton Street C0800, Austin, TX, 78712, USA

ARTICLE INFO

Article history:
Received 8 June 2015
Received in revised form 14 August 2015
Accepted 17 August 2015
Available online 20 August 2015

Keywords:
Nanoparticles
Endocytosis
Delivery
Magneto-photo-acoustic imaging

ABSTRACT

Many biomedical applications necessitate a targeted intracellular delivery of the nanomaterial to specific cells. Therefore, a non-invasive and reliable imaging tool is required to detect both the delivery and cellular endocytosis of the nanoparticles. Herein, we demonstrate that magneto-photo-acoustic (MPA) imaging can be used to monitor the delivery and to identify endocytosis of magnetic and optically absorbing nanoparticles. The relationship between photoacoustic (PA) and magneto-motive ultrasound (MMUS) signals from the in vitro samples were analyzed to identify the delivery and endocytosis of nanoparticles. The results indicated that during the delivery of nanoparticles to the vicinity of the cells, both PA and MMUS signals are almost linearly proportional. However, accumulation of nanoparticles within the cells leads to nonlinear MMUS-PA relationship, due to non-linear MMUS signal amplification. Therefore, through longitudinal MPA imaging, it is possible to monitor the delivery of nanoparticles and identify the endocytosis of the nanoparticles by living cells.

1. Introduction

With a size of about 100 to 10000 times smaller than human cells, nanoparticles offer unprecedented potentials to interact with biomolecules and to revolutionize disease diagnosis and treatment. As an example, nanoparticles have recently attracted significant attention as the vehicle to deliver and release drugs and therapeutic agents to the disease site [9,28] to achieve highly localized therapeutic strategies. Such localized therapeutic applications ultimately necessitate a targeted intracellular delivery and availability of the nanoparticles to specific target cells [7,9,28]. The interaction between nanoparticles and target cells often includes two steps: delivery and accumulation. During the delivery step, the nanoparticles (administrated through the blood stream or directly injected to the site of interest) are delivered to the vicinity of target cells via different mechanism such as enhanced permeability and retention (EPR) effect [36]. Second, the delivered nanoparticles accumulate within the target cells through endocytosis, which is one of the primary membrane translocation mechanisms for nanoparticles entry into the living cells [15]. Fully understanding the interactions between nanoparticles and cells is an enormous advancement towards evaluating the utility of molecularly targeted nanoparticles in both diagnostic and therapeutic applications. In an ideal scenario, nanoparticles which are utilized as biosensors must be activated or generate signal only when they have entered the cells through endocytosis. However, in real applications, signals are generated not only from the endocytosed nanoparticles but also from the nanoparticles in the vicinity of the cells; and it is extremely difficult to differentiate between these signals. Most molecular imaging modalities have limited sensitivity and resolution to specifically sense the endocytosis of nanoparticles into living cells mostly due to similar signature of the obscuring signal generated by the delivered yet not endocytosed nanoparticles [4,43]. Therefore, imaging strategies capable of detecting nanoparticle delivery and sensing of their intracellular endocytosis is highly desirable.

Magneto-photo-acoustic (MPA) imaging was developed based on the integration of ultrasound (US) [6], photoacoustic (PA) [3,13,27,39,41], and magneto-motive ultrasound (MMUS) [18–22,26] imaging modalities [11,31–33,35]. By utilizing magneto-plasmonic nanoparticles as imaging contrast agent, MPA can provide imaging information at cellular and molecular level with a high resolution and sensitivity [10,33]. In our previous studies, we

* Corresponding author.
E-mail addresses: mehr@wayne.edu (M. Mehrmohammadi), emelian@utexas.edu, stas@gatech.edu (S.Y. Emelianov).
[1] Current address: Department of Biomedical Engineering, Wayne State University, 818 W Hancock Street, Detroit, MI 48201.
[2] Current address: School of Electrical and Computer Engineering and Department of Biomedical Engineering, Georgia Institute of Technology and Emory University School of Medicine, 777 Atlantic Drive, Atlanta, GA 30332.

http://dx.doi.org/10.1016/j.pacs.2015.08.004

have reported a phenomenon that the intracellular accumulation of magnetic nanoparticles generates larger MMUS signals than the same concentration of isolated nanoparticles [22,23]. Furthermore, we demonstrated that MPA imaging could differentiate between the isolated nanoparticles in the vicinity of the cells and the accumulated nanoparticles within the cells [34]. In MPA imaging, the amplitude of the PA signal is proportional to the concentration of optical absorbers, i.e. magneto-plasmonic nanoparticles. Although accumulation of plasmonic metallic nanoparticles could increase the local heating effect and thus introduces linear and even nonlinear amplification of PA signal in aggregated and accumulated nanoparticles [25], such phenomenon may not happen for some types of nanoparticles such as dye-doped silica-coated magnetic particles [1,24]. On the other hand, when such nanoparticles are endocytosed, confined in lysosomes, and form intracellular aggregates with much larger size than isolated nanoparticles [5,8,12,38], the MMUS signal is amplified significantly. In other words, the MMUS signal from nanoparticles depends on both the concentration of nanoparticles and their functional state (i.e., isolated or endocytosed/aggregated) [22,23]. Therefore, the ratio between MMUS and PA (MMUS/PA) signals represents the magnetically induced motion from the unit concentration of nanoparticles. Such ratio, monitored over time, could identify both the delivery of nanoparticles and endocytosis of nanoparticles by cells.

Our previous work provided an initial framework for non-invasive detection of endocytosis of nanoparticles using MPA imaging [34]. In the current study, we further evaluate the utility of MPA imaging, coupled with an analytical method, to monitor nanoparticle delivery and to detect the endocytosis process. Herein, we propose a longitudinal analysis of MPA signal to monitor accumulation and endocytosis of nanoparticles within the cells. To achieve this goal, cell-tissue mimicking phantoms were designed to closely mimic the realistic in vivo scenario, in which some of the nanoparticles were endocytosed by the cells of interest, while the rest of the isolated nanoparticles were present in the vicinity of the cells. Two in vitro sets of experiments were designed to simulate the delivery and endocytosis of nanoparticles. The MPA imaging experiments were performed and the relationship between PA and MMUS signals were analyzed to identify the delivery and cellular accumulation processes.

2. Materials and Methods

2.1. Synthesis of magnetic nanoparticles as MPA contrast agents

Citrate-capped magnetite (Fe_3O_4) nanoparticles with optical absorption at the visible wavelength and large magnetic susceptibility (56 emu/gr Fe) were used as contrast agent in our MPA imaging studies. The citrate-capped Fe_3O_4 nanoparticles were synthesized through a phase transfer reaction between tri(ethylene glycol)-coated Fe_3O_4 nanoparticles in ethanol and an aqueous solution of 14 mg/mL sodium citrate (Sigma-Aldrich) in nano-pure water [33,37]. The volume ratio between the tri(ethylene glycol)-coated Fe_3O_4 solution and the sodium citrate was 1:1. The tri(ethylene glycol)-coated Fe_3O_4 nanoparticles were synthesized by the thermal decomposition of 1 g of iron (III) acetylacetonate ($\geq$99.9% trace metals basis, Sigma-Aldrich) in 20 mL tri(ethylene glycol) (Sigma-Aldrich) at ~250 °C for four hours (Maity et al., 2009). Prior to the phase transfer reaction, the obtained tri(ethylene glycol)-coated Fe_3O_4 nanoparticles were cleaned in 0.25 mL batches. A mixture of 0.25 mL Fe_3O_4 nanoparticles, 0.75 mL ethanol, and 1 mL ethyl acetate was centrifuged at 14,000 g for half an hour. A black NP pellet was obtained after decanting the supernatant. The cleaning step was repeated three times, and the obtained pellet of cleaned Fe_3O_4 nanoparticles was re-suspended in 0.25 mL ethanol. Then, the desired volumes of cleaned Fe_3O_4 nanoparticles in ethanol and the sodium citrate in water solution were mixed together and shaken at 500 rpm overnight, allowing the phase transfer reaction. In this reaction, the Fe_3O_4 nanoparticles' tri(ethylene glycol) surface layer was replaced with citrate ions. The citrate-capped Fe_3O_4 nanoparticles were obtained by centrifuging the reaction solution in Millipore 50 kDa Amicon Ultra-15 Centrifugal Filter Units at 3,000 g for 15 minutes. The obtained nanoparticles were re-suspended with nano-pure water and re-filtered four times. Finally the filtered citrate-capped Fe_3O_4 nanoparticles were re-suspended in 1 × PBS solution. The size of the synthesized Fe_3O_4 nanoparticles were measured as approximately 7.5 nm by using a transmission electron microscope (Fig. 1A). As shown previously, the Fe_3O_4 nanoparticles possessed strong optical absorption in visible wavelengths and high magnetic susceptibility [33]. In this study, the synthesized SPIO nanoparticles does not show plasmonic effect that can potentially interfere with hypothesis behind this study. These contrast agents do not have absorption peak within near infrared (NIR) region and absorb relatively high at 532 nm. Therefore, PA imaging experiments were performed at 532 nm wavelength.

2.2. Cell-nanoparticles tissue mimicking phantoms

The macrophages (J774 A1) cells were incubated with citrate-capped Fe_3O_4 nanoparticles for 24 hours. Then the harvested macrophages were washed three times with phosphate buffered saline (PBS). Cellular uptake, measured using inductively coupled plasma mass spectrometry (ICP-MS), was approximately 6.7×10^6 citrate-capped Fe_3O_4 nanoparticles (7.65 pg Fe_3O_4 nanoparticles) per cell. The TEM image of macrophages with endocytosed nanoparticles is shown in Fig. 1(B).

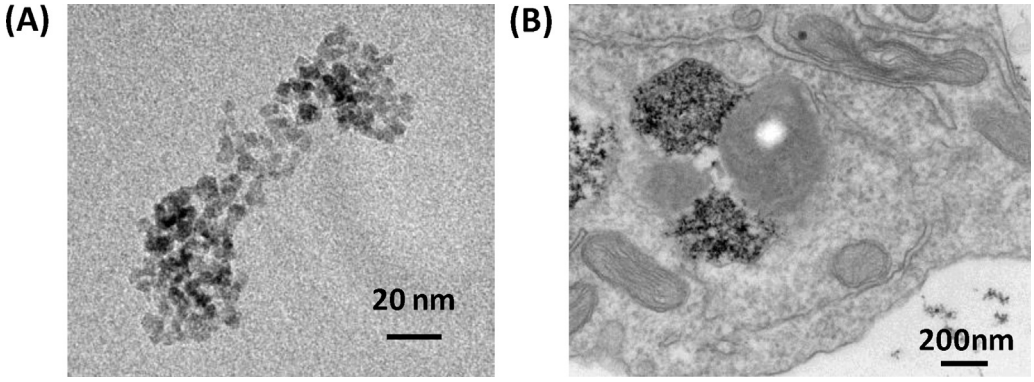

Fig. 1. Transmission electron microscopy (TEM) image of (A) Fe_3O_4 nanoparticles, (B) macrophages with endocytosed Fe_3O_4 nanoparticles.

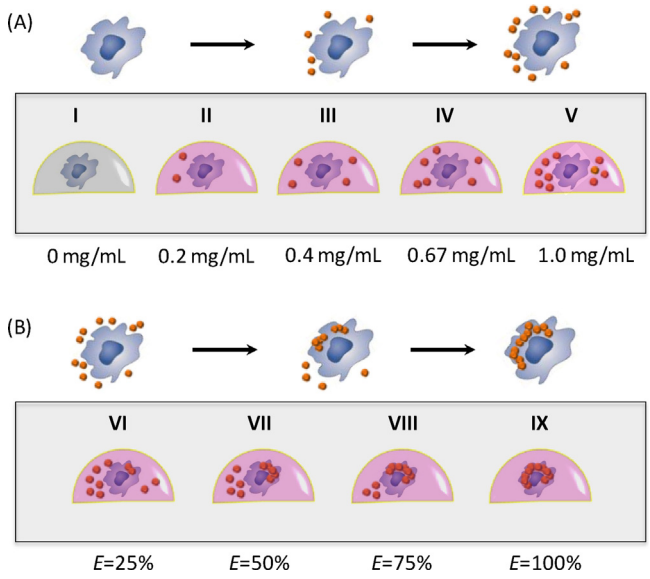

Fig. 2. (A) First phantom with inclusions was designed to mimic delivery of nanoparticles. Inclusion I was used as control. Other inclusions contained different concentrations of isolated Fe_3O_4 nanoparticles. (B) Second phantom was designed to mimic endocytosis of nanoparticles. Parameter E represented the endocytosis ratio, which was defined as the ratio of the number of endocytosed nanoparticles to the total number of nanoparticles in tissue (both endocytosed nanoparticles and isolated nanoparticles in the vicinity of cells). Inclusions VI to IX mimicked different portions of nanoparticles were endocytosed by living cells.

Two tissue-mimicking gelatin phantoms were prepared to simulate the delivery and endocytosis processes of nanoparticles (Fig. 2). The background of the tissue-mimicking phantoms was made out of 3 wt/wt gelatin (300 bloom, Sigma Aldrich, MO, USA). The inclusions were prepared by mixing 3 wt/wt gelatins with Fe_3O_4 nanoparticles at different concentrations or functional states (i.e., endocytosed Fe_3O_4 nanoparticles, isolated nanoparticles, or mixture of both). In the first phantom, inclusions I to V contained non-labeled cells mixed with different concentrations of isolated Fe_3O_4 nanoparticles, mimicking NP delivery into tissues. Inclusion I contained macrophage cells only and served as control; the remaining inclusions contained 0.2 mg/mL (inclusion II), 0.4 mg/mL (inclusion III), 0.67 mg/mL (inclusion IV), and 1 mg/mL (inclusion V) Fe_3O_4 nanoparticles mixed with cells.

The second phantom was made to simulate the endocytosis process. The endocytosis process can be considered as a two-stage process. In the first stage, the nanoparticles are delivered to the vicinity of cells and then in second stage, they are endocytosed by the cells. To simulate this process, two set of cells were prepared: (a) cells loaded with nanoparticles, and (b) intact (unloaded) cells. Knowing the average number of nanoparticles in loaded cells (through ICP-MS measurements), four inclusions were made out of gelatin and mixture of nanoparticles and magnetically labeled cells. While the concentration of magnetite nanoparticles was kept the same in all four inclusions, the ratio between the endocytosed nanoparticles (contained in labeled cells) and the isolated nanoparticles was different. For example, in phantom VI, 25% of total nanoparticles were within the loaded cells, and the rest were simply mixed with intact cells. Therefore, inclusions XI to IX have the same number or concentration of nanoparticles as well as the same number of cells. However, the portion of nanoparticles within the cells and mixed with the cells were changed. The different ratios mimicked the cellular uptake of nanoparticles by living cells in vivo. The parameter E in Fig. 2(B) represents the percentage of endocytosis and defined as:

$$E = \frac{Number\ o\ f\ endocytosed\ nano\ particles}{Total\ number\ o\ f\ nano\ particles(endocytosed + isolated)} \times 100\%$$

The total number of Fe_3O_4 nanoparticles within the inclusions include both endocytosed nanoparticles inside cells and isolated nanoparticles in the vicinity of cells. The increase of E indicates the larger uptake of nanoparticles by the macrophage cells. Parameter E was precisely controlled and varied between 25% to 100% with an increment of 25%. As a result, inclusions VI, VII, VIII, and IX contain 25%, 50%, 75%, and 100% of nanoparticles in endocytosed functional state. To eliminate any experimental dependent variation in MPA measurements, an identical number of macrophage cells (3.75×10^6 cells) was embedded in all inclusions. In addition, 0.2 wt% of 30 μm silica particles, acting as ultrasound scatters, was added to the inclusions.

2.3. MPA imaging

To evaluate the ability of MPA imaging to assess nanoparticles endocytosis process, MPA imaging system shown in Fig. 3 was used to image tissue-mimicking phantoms. Samples were placed in a water cuvette that was attached to a 3D positioning stage. The laser

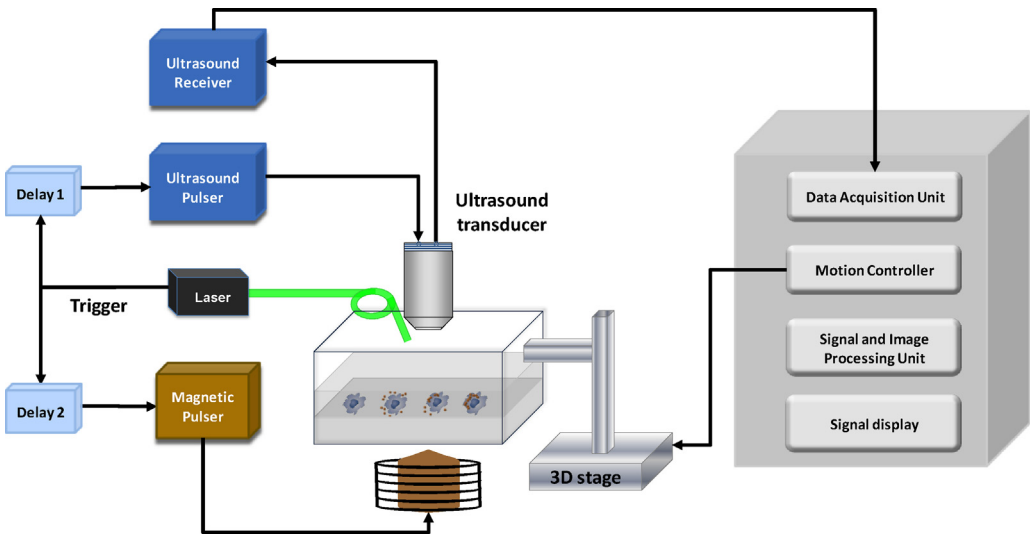

Fig. 3. Magneto-photo-acoustic (MPA) imaging system block diagram including ultrasound pulser/receiver, laser and magnetic excitation.

source was a tunable optical parametric oscillator (OPO, Spectra-Physics) laser system (400~2600 nm wavelength range, 5~7 ns pulse duration, up to 10 Hz pulse repetition frequency). The pulsed laser light at 532 nm wavelength was delivered to the samples through a 1500 μm diameter optical fiber. The fluence of the laser was measured as 10 mJ/cm^2 with power meter (Nova II, Ophir Ltd., Jerusalem, Israel). A single-element focused US transducer (25 MHz center frequency, bandwidths of about 50%, 25.4 mm focal depth, f-number of 4, Olympus-NDT, Waltham, MA, USA) was used for pulse-echo US imaging as well as for PA signal detection. The imaging sequence was set as following. First, the PA signal is generated and detected by the US transduce. After a delay of 30 μs, US pulse was sent to the sample and the backscattered US echo signal was detected to form US image. Then a pulsed magnetic field with 20 ms pulse duration was applied from the bottom of the sample through a solenoid with a cone-shaped-tip core to focus the field to induce the magneto-motive displacement. The magnetic flux density (B) was measured as 0.8 T at the tip of a cone shaped core embedded within the coil by using a digital Gaussmeter (DSP 475, Lakeshore Crytronics, OH, USA). The air gap between the water tank and iron core tip was about 1 mm to avoid any direct contact between the sample and magnetic field generator. The US pulse-echo signals were acquired to track the magnetically induced displacement from the sample. The repetition rate of the US pulses sent to the sample was 1 kHz. A total of 100 pulse-echoes (100 ms) were acquired for the displacement tracking, in which 20 pulse-echoes (20 ms) were measured before the application of the magnetic field and used as the static reference of motion detection. After the magnetic excitation, 80 pulse-echo signals over 80 ms time interval were acquired to track the magnetically induced. At each data point, the temporal behavior of the displacement was calculated by estimating the cross-correlation between the static signal and the signals acquired after the magnetic field application [17]. The maximum measured displacement was used to form MMUS image. A custom-built LabVIEW (National Instruments, TX, USA) application was used to control the mechanical scanning to provide spatially co-registered US, PA and MMUS images.

The US, PA and MMUS images of inclusions within each tissue-mimicking phantom were reconstructed and spatially co-registered. To further analyze the ability of MPA imaging to detect the delivery of nanoparticles and endocytosis, the regions of interest of the same size were selected within each inclusion. The amplitude of PA and MMUS signal was averaged within each region of interest. Then the PA signal was plotted versus MMUS signal for each inclusions, and the realationship between both signals was studied. Specifically, based on the linear fitting, the slopes of PA-MMUS curves for the inclusions within phantoms were compared to indicate the processes of delivery and celluar endocytosis.

3. Results and Discussion

The US images of the first phantom, which mimicked the delivery of nanoparticles to the vicinity of cells, are shown in Fig. 4(A). The averaged amplitude of the PA signal from each inclusion (marked with yellow semicircle) is displayed in Fig. 4B. The error bars in Fig. 4B show the standard deviation of the PA signal magnitude from multiple measurements. There was no significant PA signal detected from inclusion I, which did not contain any Fe_3O_4 nanoparticles and was used as a control. The PA signals from inclusions II to V indicate that the amplitude of PA signals increased proportional to the concentration of nanoparticles. This result is consistent with the linear dependence of PA signals on the concentration of nanoparticles (gold nanorods) shown in previous studies [34]. The magnetically induced displacement was measured from the regions outlined with red rectangle (1000 μm axially and 500 μm laterally) in each inclusion. The mean and standard deviation of MMUS signal from each inclusion are displayed in Fig. 4C. As the concentration of nanoparticles increases, the magnetically induced displacement increases. Finally, the relationship between PA and MMUS signals is shown in Fig. 4D. In Fig. 4D, the PA signal amplitude is shown in vertical axis, while the amplitude of MMUS signal is shown in horizontal axis. The fitting curve of PA-MMUS plot indicates the linear relationship between PA and MMUS signals for the isolated nanoparticles. In other words, when the nanoparticles are delivered into the tissue, both PA and MMUS signal showed a monotonic increase with respect to the concentration of nanoparticles. Therefore, a positive slope of PA-MMUS curve was associated with the delivery process.

The US images of the inclusions in second phantom, which mimicked the endocytosis of nanoparticles by the living cells, are shown in Fig. 5(A). Four inclusions contained the same concentration of Fe_3O_4 nanoparticles (0.67 mg/mL) with different endocytosis ratio E. The E value for inclusions VI, VII, VIII, and IX was 25%, 50%, 75%, and 100%, respectively. Similar to the previous phantom, PA and MMUS signals, as well as their ratio for different inclusions, were measured and analyzed (Fig. 5B-D). PA signals from all the inclusions were approximately the same, which was expected given the same concentration of nanoparticles in all inclusions

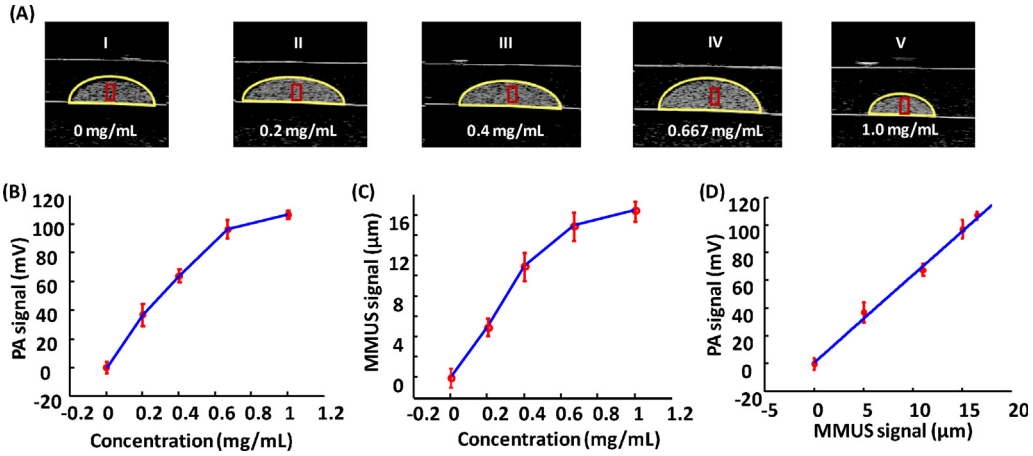

Fig. 4. (A) US images of the inclusions within the delivery-mimicking phantom. Each image is 8.09 mm axially. (B) Relationship between the PA signal amplitude from the region marked with yellow semicircle and the concentration of Fe_3O_4 nanoparticles. (C) Relationship between the MMUS signal amplitude from the regions marked with red rectangle and the concentration of Fe_3O_4 nanoparticles. (D) Relationship between MMUS signals and PA signals as Fe_3O_4 nanoparticles were delivered into tissues.

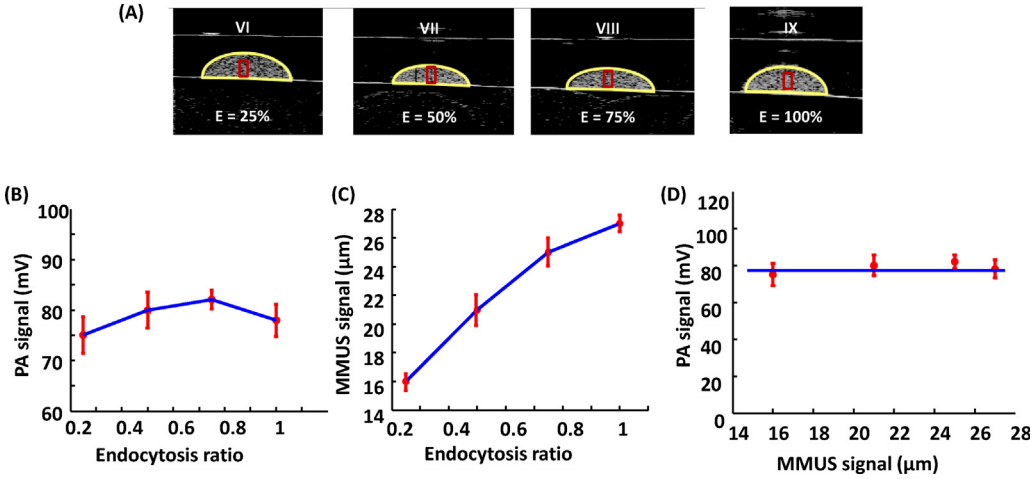

Fig. 5. (A) US images of the inclusions within the endocytosis-mimicking phantom. (B) The relationship between the PA signal amplitude from the region marked with yellow semicircle and the endocytosis ratio E of Fe_3O_4 nanoparticles. (C) The relationship between the MMUS signal amplitude from the regions marked with red rectangle and endocytosis ratio E of Fe_3O_4 nanoparticles. (D) The relationship between MMUS signals and PA signals as Fe_3O_4 nanoparticles were endocytosed by living cells.

[34]. On the other hand, the MMUS signal (i.e. magnetically induced displacement) increased significantly when E value was larger, indicating more nanoparticles entered into cells. Thus MMUS signal was sensitive to the endocytosis process (Fig. 5C). Finally the relationship between PA and MMUS signals (Fig. 5D) shows a different trend compared to the delivery process. As more Fe_3O_4 nanoparticles were endocytosed, the PA signal remained constant while the MMUS signal increased. Therefore, the slope of the PA – MMUS curve was zero during the endocytosis process.

The results shown in Figures 4 and 5 suggest that MPA imaging is capable of monitoring the delivery and intracellular endocytosis of nanoparticles. During the nanoparticles' delivery, the concentration of nanoparticles increases, and both PA and MMUS signals increase linearly. Thus a linear relationship between PA and MMUS signals was observed (Fig. 4D). In the process of nanoparticles' endocytosis, assuming the concentration of nanoparticles remains constant, PA signal is relatively constant, while the MMUS signal is amplified due to the aggregation of endocytosed nanoparticles within the endosomes [5,8,12,22,34,38]. Thus the slope of PA-MMUS curve is zero for endocytosis process. Therefore, nanoparticles' delivery and endocytosis can be detected by investigating the relationship between PA and MMUS signals. Such ability of MPA imaging could be advantageous for several biomedical applications of nanoparticles such as drug delivery [14], cancer therapy [29], biosensors [16].

From above results, at the same concentration of nanoparticles, the amplitude of MMUS signal is directly related to the ratio of endocytosed nanoparticles. In MMUS imaging, the magnetomotive force (F) acting on a magnetic NP that causing the displacement can be expressed as

$$F(Z) = \frac{V_{np} f_m \chi_{np}}{\mu_0} B_Z \frac{\partial B_Z}{\partial z} \quad (1)$$

where V_{np} is the total size of the NP, f_m is a dimensionless factor that represents the volumetric ratio of magnetic material in a NP, z is the direction along the magnetic field, μ_0 is vacuum permeability, B_z is magnetic flux density, and χ_{np} is the volume magnetic susceptibility of the NP. From Equation (1), the induced MMUS signal is proportional to the magnetic susceptibility of the NPs. For dilute solution of magnetic particles, the magnetic susceptibility is proportional to particle concentration [2] However, as particle concentration increases, the magnetic susceptibility increases faster than linear dependence due to the interaction between the particles [30]. Especially, when aggregates were formed, a significant non-linear amplification was observed in magnetic susceptibility, resulting in larger MMUS signals [22]. MMUS imaging is sensitive to detect aggregations containing several Fe_3O_4 NPs [22]. When nanoparticles were endocytosed by the cells, the aggregates, formed within lysosomal bodies, contain several to tens of nanoparticles [5,8,12,38] (Fig. 1). The interaction between the Fe_3O_4 NPs in the aggregate resulted in larger susceptibility and increased MMUS signals. Therefore, the larger magnetically induced displacement from the endocytosed NPs compared to that from the same concentration of isolated NPs is due to the interaction between magnetic NPs.

Longitudinal MPA imaging has the potential to monitor the delivery and endocytosis of nanoparticles in vivo. When nanoparticles are injected locally or systemically, they will accumulate in the site of interest and be present in the vicinity of the cells at first, Then the NPs will be endocytosed by the cells and form aggregates in membrane vesicles. The analysis of PA-MMUS curve over time is indicative of each stage of the process. When the nanoparticles start accumulating, the PA-MMUS curve would exhibit a positive slope, considering the dependence of both PA and MMUS signals on the concentration of nanoparticles. When certain amount of nanoparticles is accumulated, some of them enter into the cells through endocytic process, and the MMUS signal would increase nonlinearly. Thus, the slope of PA-MMUS will reduce. Finally, when a delivery equilibrium is achieved, the concentration of nanparticles in the region of interest will not change while more nanoparticles will be endocytosed by the cells. In tis case, the PA signal will be constant, while the MMUS signal will keep increasing due to stronger MMUS response from the endocytosed nanoparticles. Thus the PA-MMUS curve will have a zero slope for this stage. Therefore, without a prior information, longitunal MPA imaging along should be able to monitor the delivery and endocytosis processes non-invasively in vivo.

In the current in vitro study, Fe_3O_4 nanoparticles were used as contrast agent for both PA and MMUS imaging, given their biocompatibility and availability, to investigate the interaction between nanoparticles with macrophage cells. For further advanced applications, magneto-plasmonic nanoconstructs could be used as contrast agents for the MPA imaging [40,42]. Coupling with the capability of MPA imaging to sense endocytosed nanoparticles, the dual-contrast nanoparticles could be used as biosensors in living cells.

4. Conclusions

In conclusion, this study demonstrated that the delivery and cellular endocytosis of nanoparticles can be noninvasively sensed by MPA imaging. In MPA imaging, the relationship between PA and MMUS signals was analyzed to be indicative of the functional processes of nanoparticles in tissue. When the nanoparticles were delivered into tissue, both PA and MMUS signals increased linearly to the NP concentration. On the other hand, when the nanoparticles entered into living cells based on endocytosis, the PA signal remained relatively constant while the MMUS signal was amplified. Therefore, the slope of MMUS-PA curve can provide information on the delivery and endocytosis processes of the nanoparticles.

Conflict of interest

The authors declare that there are no conflicts of interest.

Acknowledgements

The authors are grateful to Dr. Dwight K. Romanovicz from Institute for Cellular and Molecular Biology at the University of Texas at Austin for his help with transmission electron microscopy of cells, and to Mr. Ryan Truby of the University of Texas at Austin (currently at Harvard University) for synthesis of the magnetite nanoparticles. This work was partially supported by the National Institutes of Health under grant EB 008821.

References

[1] C.L. Bayer, Y.-S. Chen, S. Kim, S. Mallidi, K. Sokolov, S. Emelianov, Multiplex photoacoustic molecular imaging using targeted silica-coated gold nanorods, Biomedical Optics Express 2 (2011) 1828–1835.
[2] B. Berkovsky, V.F. Medvedev, M.S. Krakov, Magnetic fluids, Oxford University Press, 1993.
[3] T. Bowen, R. Nasoni, A. Pifer, G. Sembroski, Some experimental results on the thermoacoustic imaging of tissue equivalent phantom materials, Ultrasonics Symposium (1981) 823–827.
[4] W. Cai, X. Chen, Nanoplatforms for targeted molecular imaging in living subjects, Small 3 (2007) 1840–1854.
[5] B.D. Chithrani, W.C. Chan, Elucidating the mechanism of cellular uptake and removal of protein-coated gold nanoparticles of different sizes and shapes, Nano Letters 7 (2007) 1542–1550.
[6] F.S. Foster, G. Lockwood, L. Ryan, K. Harasiewicz, L. Berube, A. Rauth, Principles and applications of ultrasound backscatter microscopy IEEE Transactions on Ultrasonics, Ferroelectrics and Frequency Control 40 (1993) 608–617.
[7] J. Gao, B. Xu, Applications of nanomaterials inside cells, Nano Today 4 (2009) 37–51.
[8] A.K. Gupta, A.S. Curtis, Surface modified superparamagnetic nanoparticles for drug delivery: interaction studies with human fibroblasts in culture, Journal of Materials Science: Materials in Medicine 15 (2004) 493–496.
[9] X. Huang, I.H. El-Sayed, W. Qian, M.A. El-Sayed, Cancer cell imaging and photothermal therapy in the near-infrared region by using gold nanorods, J. Am. Chem. Soc 128 (2006) 2115–2120.
[10] Y. Jin, C. Jia, S.-W. Huang, M. O'Donnell, X. Gao, Multifunctional nanoparticles as coupled contrast agents, Nature communications 1 (2010) 41.
[11] Y. Jin, C. Jia, S.W. Huang, M. O'Donnell, X. Gao, Multifunctional nanoparticles as coupled contrast agents, Nature Communications 1 (2010) 1–8.
[12] J. Kneipp, H. Kneipp, M. McLaughlin, D. Brown, K. Kneipp, In vivo molecular probing of cellular compartments with gold nanoparticles and nanoaggregates, Nano Letters 6 (2006) 2225–2231.
[13] R.A. Kruger, P. Liu, Photoacoustic ultrasound: pulse production and detection in 0.5% liposyn, Medical physics 21 (1994) 1179.
[14] L. Hu, W. Mao Z, C.Y. Gao, Colloidal particles for cellular uptake and delivery, J Mater Chem 19 (2009) 3108–3115.
[15] R. Lévy, U. Shaheen, Y. Cesbron, V. Sée, Gold nanoparticles delivery in mammalian live cells: a critical review, Nano Reviews 1 (2010) 1–18.
[16] H. Lord, S.O. Kelley, Nanomaterials for ultrasensitive electrochemical nucleic acids biosensing, J Mater Chem 19 (2009) 3127–3134.
[17] M. Lubinski, S. Emelianov, M. O'Donnell, Speckle tracking methods for ultrasonic elasticity imaging using short-time correlation IEEE Transactions on Ultrasonics, Ferroelectrics and Frequency Control 46 (2002) 82–96.
[18] M. Mehrmohammadi, J. Oh, S.R. Aglyamov, A.B. Karpiouk, S.Y. Emelianov, Pulsed magneto-acoustic imaging: IEEE (2009) 4771–4774.
[19] M. Mehrmohammadi, J. Oh, L. Ma, E. Yantsen, T. Larson, S. Mallidi, S. Park, K.P. Johnston, K. Sokolov, T. Milner, S. Emelianov, Imaging of iron oxide nanoparticles using magneto-motive ultrasound, IEEE Ultrasonics Symposium (2007) 652–655.
[20] M. Mehrmohammadi, J. Oh, S. Mallidi, S.Y. Emelianov, Pulsed magneto-motive ultrasound imaging using ultrasmall magnetic nanoprobes, Molecular imaging 10 (2011) 102.
[21] M. Mehrmohammadi, T.-H. Shin, M. Qu, P. Kruizinga, R.L. Truby, J.-H. Lee, J. Cheon, S.Y. Emelianov, In vivo pulsed magneto-motive ultrasound imaging using high-performance magnetoactive contrast nanoage, Nanoscale 5 (2013) 11179–11186.
[22] M. Mehrmohammadi, K. Yoon, M. Qu, K. Johnston, S. Emelianov, Enhanced pulsed magneto-motive ultrasound imaging using superparamagnetic nanoclusters, Nanotechnology 22 (2011) 045502.
[23] M. Mehrmohammadi, K.Y. Yoon, M. Qu, K.O. Johnston, S.Y. Emelianov, On application of magnetic nanoclusters to improve the sensitivity of pulsed magnetomotive ultrasound imaging, Ultrasonics Symposium (IUS), 2010 IEEE (2010) 241–244.
[24] S.Y. Nam, L.M. Ricles, L.J. Suggs, S.Y. Emelianov, In vivo ultrasound and photoacoustic monitoring of mesenchymal stem cells labeled with gold nanotracers, PLoS One 7 (2012) e37267.
[25] S.Y. Nam, L.M. Ricles, L.J. Suggs, S.Y. Emelianov, Nonlinear photoacoustic signal increase from endocytosis of gold nanoparticles, Optics letters 37 (2012) 4708–4710.
[26] J. Oh, M.D. Feldman, J. Kim, C. Condit, S. Emelianov, T.E. Milner, Detection of magnetic nanoparticles in tissue using magneto-motive ultrasound, Nanotechnology 17 (2006) 4183–4190.
[27] A.A. Oraevsky, S.L. Jacques, R.O. Esenaliev, F.K. Tittel, Laser-based optoacoustic imaging in biological tissues, Proc SPIE 2134 (1994) 122.
[28] J. Panyam, V. Labhasetwar, Biodegradable nanoparticles for drug and gene delivery to cells and tissue, Advanced Drug Delivery Reviews 55 (2003) 329–347.
[29] D. Peer, J.M. Karp, S. Hong, O.C. FaroKhzad, R. Margalit, R. Langer, Nanocarriers as an emerging platform for cancer therapy, Nat Nanotechnol 2 (2007) 751–760.
[30] A. Pshenichnikov, Equilibrium magnetization of concentrated ferrocolloids, Journal of magnetism and magnetic materials 145 (1995) 319–326.
[31] M. Qu, S. Kim, M. Mehrmohammadi, S. Mallidi, P. Joshi, K. Homan, Y.S. Chen, S. Emelianov, Combined photoacoustic and magneto-motive ultrasound imaging 7564 (2010) 756433–756441.
[32] M. Qu, S. Mallidi, M. Mehrmohammadi, L.L. Ma, K.P. Johnston, K. Sokolov, S. Emelianov, Combined photoacoustic and magneto-acoustic imaging: IEEE (2009) 4763–4766.
[33] M. Qu, S. Mallidi, M. Mehrmohammadi, R. Truby, K. Homan, P. Joshi, Y.S. Chen, K. Sokolov, S. Emelianov, Magneto-photo-acoustic imaging, Biomed Opt. Express 2 (2011) 385–395.
[34] M. Qu, M. Mehrmohammadi, S. Emelianov, Detection of nanoparticle endocytosis using magneto-photoacoustic imaging, Small 7 (2011) 2858–2862.
[35] M. Qu, M. Mehrmohammadi, R. Truby, I. Graf, K. Homan, S. Emelianov, Contrast-enhanced magneto-photo-acoustic imaging in vivo using dual-contrast nanoparticles, Photoacoustics 2 (2014) 55–62.
[36] E. Ruoslahti, S.N. Bhatia, M.J. Sailor, Targeting of drugs and nanoparticles to tumors, The Journal of cell biology 188 (2010) 759–768.
[37] R.L. Truby, K.A. Homan, M. Qu, M. Mehrmohammadi, S. Emelianov, Synthesis of a hybrid plasmonic-superparamagnetic contrast agent for magneto-photo-acoustic imaging, Biomecial Engineering Society Annual Meeting (2010).
[38] A. Verma, F. Stellacci, Effect of surface properties on nanoparticle–cell interactions, Small 6 (2010) 12–21.
[39] B. Wang, E. Yantsen, T. Larson, A.B. Karpiouk, S. Sethuraman, J.L. Su, K. Sokolov, S.Y. Emelianov, Plasmonic intravascular photoacoustic imaging for detection of macrophages in atherosclerotic plaques, Nano Letters 9 (2009) 2212–2217.
[40] C. Wang, J. Chen, T. Talavage, J. Irudayaraj, Gold nanorod/Fe3O4 nanoparticle "nano-pearl-necklaces" for simultaneous targeting, dual-mode imaging, and photothermal ablation of cancer cells, Angewandte Chemie 121 (2009) 2797–2801.
[41] X. Wang, Y. Pang, G. Ku, X. Xie, G. Stoica, L.V. Wang, Noninvasive laser-induced photoacoustic tomography for structural and functional in vivo imaging of the brain, Nature Biotechnology 21 (2003) 803–806.
[42] Q. Wei, H.M. Song, A.P. Leonov, J.A. Hale, D. Oh, Q.K. Ong, K. Ritchie, A. Wei, Gyromagnetic imaging: dynamic optical contrast using gold nanostars with magnetic cores, Journal of the American Chemical Society 131 (2009) 9728–9734.
[43] R. Weissleder, M.J. Pittet, Imaging in the era of molecular oncology, Nature 452 (2008) 580–589.

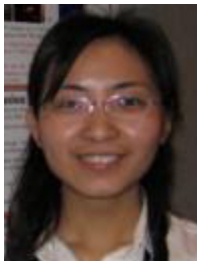

Min Qu received her B.S. and M.S. degrees in Electrical Engineering at Nanjing University in China, in 2005 and 2008, respectively. She received her Ph.D. degree in Biomedical Engineering at the University of Texas at Austin in TX in 2011. She is currently an applied research engineer in Biotronik Inc. in Portland, OR. Her research interests include ultrasound-based hybrid imaging technique, sensing functional processes of nanoparticles, and remote communication of implanted devices.

Mohammad Mehrmohammadi received his B.S. and M.S. degree in Electrical Engineering from Sharif University of Technology (Iran) and Illinois Institute of Technology (Chicago, IL) respectively. He received his Ph.D. degree in Biomedical Engineering at the University of Texas at Austin and worked as a senior research fellow at Mayo Clinic in Rochester, Minnesota. He is currently an Assistant Professor of Biomedical Engineering at Wayne State University (Detroit, Michigan). His research interests include pre-clinical and clinical ultrasound-based molecular imaging modalities including Photoacoustic and Magneto-motive Ultrasound Imaging as well as ultrasound tissue elastography.

Stanislav Emelianov received his B.S. and M.S. degrees in physics and acoustics in 1986 and 1989, respectively, and Ph.D. degree in physics in 1993 from Moscow State University, Russia. He is currently a Professor in the Department of Biomedical Engineering at The University of Texas at Austin in Austin, TX, and an AdjunctProfessor at the University of Texas M.D. Anderson Cancer Center in Houston, TX. His research interests include molecular imaging, photoacoustic imaging, elasticity imaging, functional imaging, tissue differentiation, image-guided therapy, and contrast agents including various nanoconstructs.